Three-dimensional morphology and elastic strain revealed in individual photoferroelectric SbSI nanowire

Elijah Schold, Zachary Barringer, Xiaowen Shi, Skye Williams, Nimish Prashant Nazirkar, Yiping Wang, Yang Hu, Jian Shi, and Edwin Fohtung*

Antimony sulfoiodide (SbSI) exhibits great promise for photovoltaic applications due to it being optically active in its ferroelectric phase. Previous studies on the SbSI system have relied largely on ensemble-averaging techniques and/or computational studies, wherein true volumetric enumeration of atomic displacement has remained ambiguous at the nanoscale. Here, we have mapped strain and the complex Bragg electronic density among the (002) planes in an individual SbSI nanowire using Bragg coherent diffractive imaging in hopes of guiding efforts to strain engineer SbSI nanostructures for photovoltaic and other optoelectronic applications. We have found that the as-grown nanowire showed sharp faceting and high crystallinity, with no evidence of point or line mechanical defects in the (002) atomic displacement map (u_{002}). There is evidence, however, of planar defects in the wire that separate regions of positive and negative shear strain (τ_{32}) where these domain walls are parallel to the (011)-type facets. Increased Bragg electronic density near the center of the nanowire shows that the nanowires could have additional dangling bonds present there, increasing the likelihood that shells could bond to the wire for strain-engineering purposes.

Impact statement

Bragg coherent diffractive imaging (BCDI) is a lensless imaging technique with promised diffraction-limited spatial resolution. The technique is susceptible to local lattice distortion and structural heterogeneities with quantitative phase information. BCDI is currently widely used in nanotechnology and materials sciences in general. This article demonstrates the application of BCDI on antimony sulfoiodide (SbSI) nanowires that harbor large shear strains due to dangling bonds and crystal-tilting. SbSI is a ferroelectric material with a relatively narrow bandgap, high pyroelectricity, optical activity, and piezoelectricity, making it a promising material for infrared detectors, actuators, and storage devices. Several elastic shear domains in the shear strain component were observed in the SbSI nanowire, leading to the potential formation of ferroelectric domains above room temperature in the nanowire. The likely elastic domains identified in the BCDI reconstructions are the consequences of the strain energy minimization, originating from the global shear present in the SbSI nanowire. Our studies open up a new avenue for local strain mapping and strain-engineering characterization of above room-temperature optoelectronic nanodevices. We envisage that BCDI characterization could be used to learn and develop crucial properties on emergent nanostructure of technological importance. Ultimately, the development and optimization of associated functional devices with real-world applications are attainable.

Introduction

Ferroelectric materials have been shown to possess large potential for advancement in optoelectronic applications.[1,2] In the past decade, the Shockley–Queisser limit for *p*–*n*-type solar cells leads to new interests in bulk photovoltaic effect (BPVE) materials.[3] Ferroelectric materials are of interest in this field as the breaking of inversion symmetry affords mechanisms such

Elijah Schold, Department of Materials Science and Engineering, Materials Research Center, Rensselaer Polytechnic Institute RPI, Troy, USA; schole3@rpi.edu
Zachary Barringer, Department of Materials Science and Engineering, Materials Research Center, Rensselaer Polytechnic Institute RPI, Troy, USA; barriz@rpi.edu
Xiaowen Shi, Department of Materials Science and Engineering, Materials Research Center, Rensselaer Polytechnic Institute RPI, Troy, USA; xwshi@nmsu.edu
Skye Williams, Department of Materials Science and Engineering, Materials Research Center, Rensselaer Polytechnic Institute RPI, Troy, USA; willis11@rpi.edu
Nimish Prashant Nazirkar, Department of Materials Science and Engineering, Materials Research Center, Rensselaer Polytechnic Institute RPI, Troy, USA; nazirn@rpi.edu
Yiping Wang, Department of Materials Science and Engineering, Materials Research Center, Rensselaer Polytechnic Institute RPI, Troy, USA; wangy33@rpi.edu
Yang Hu, Department of Materials Science and Engineering, Materials Research Center, Rensselaer Polytechnic Institute RPI, Troy, USA; huy12@rpi.edu
Jian Shi, Department of Materials Science and Engineering, Materials Research Center, Rensselaer Polytechnic Institute RPI, Troy, USA; shij4@rpi.edu
Edwin Fohtung, Department of Materials Science and Engineering, Materials Research Center, Rensselaer Polytechnic Institute RPI, Troy, USA; fohtue@rpi.edu
doi:10.1557/s43577-022-00445-9

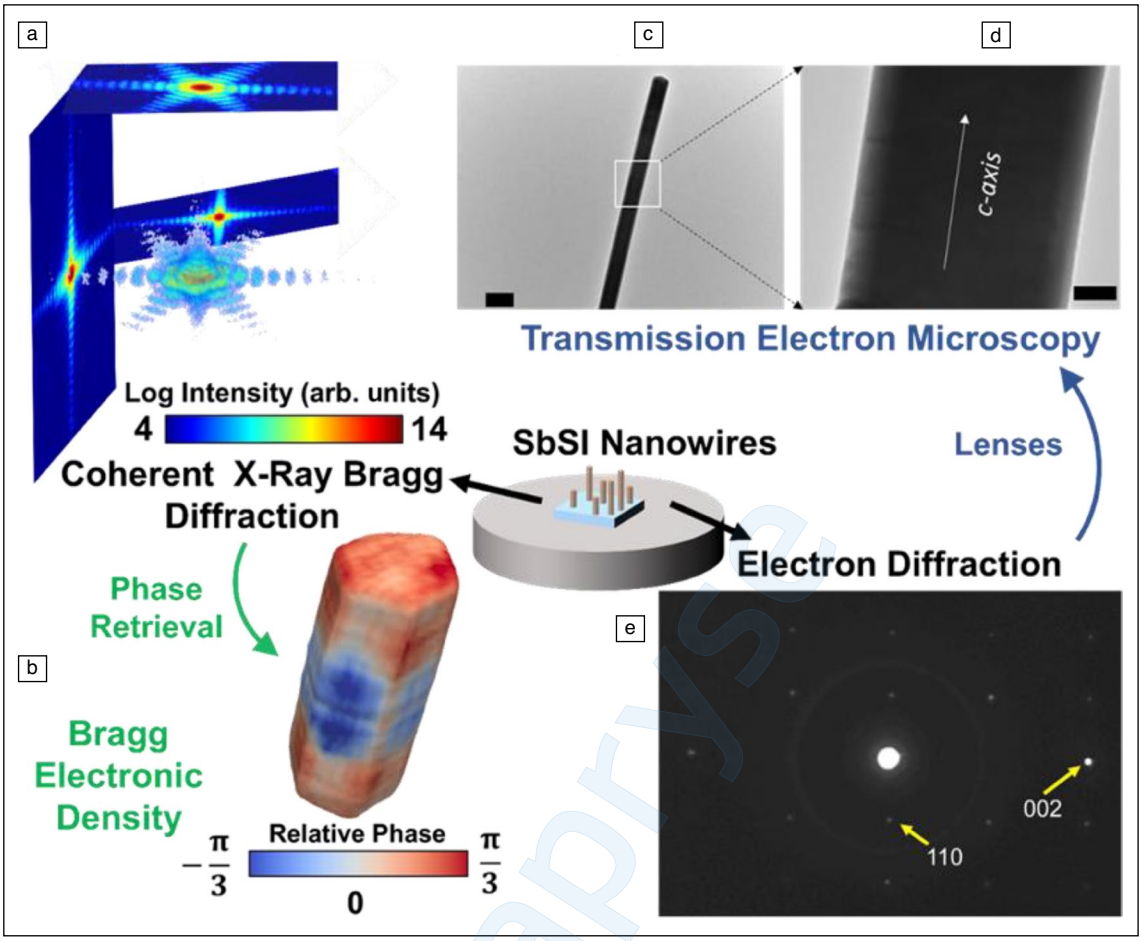

Figure 1. Comparison between two of the scattering/imaging techniques used in this study. The SbSI nanowires are randomly aligned. (a) Volumetric representation of the coherent Bragg diffraction pattern utilized in this study shown with three of its projections (log scale). (b) Complex valued reconstruction of (a), displayed as phase projected onto an isosurface of the amplitude, taken at 15% of the maximum. (c) Low-magnification transmission electron micrograph of a SbSI wire. Long axis of the wire is parallel to the *c*-axis of the SbSI unit cell. (d) High-magnification transmission electron micrograph of region in (c) indicated by the white box. (e) Selected-area diffraction pattern of the SbSI wire where $[\bar{1}10]$ is the zone axis. The diffraction pattern can be indexed based on the structure of SbSI. Scale bars = 1 μm in (c) and 100 nm in (d).

as shift current seen in BPVE materials and can lead to above-bandgap photovoltages that surpass the Shockley–Queisser limit.[4] Ferroelectric materials such as $BiFeO_3$, which have been shown to generate large above-bandgap photovoltage,[5] Bi_2FeCrO_6, which has shown a power-conversion efficiency greater than 8%,[6] and oxide ferroelectric-based photovoltaics such as photosensitive memories in $BiFeO_3$ systems[7] are examples of existing ferroelectric contributions. However, these complex oxide systems have large bandgaps, which affect their performance.

Antimony sulfoiodide (SbSI) carries ferroelectricity while maintaining a much smaller bandgap (1.43 eV indirect, 1.82 eV direct) than traditional oxide ferroelectrics (>3 eV typical).[8,9] It has high pyroelectricity,[10] optical activity in its ferroelectric phase,[11,12] and piezoelectricity,[13,14] making it a promising material system for infrared detectors, actuators, and storage devices. SbSI has shown effective use in gas detectors,[15] flexible photodetectors,[16] photocatalysis,[17] and in solar cells.[14] SbSI can also be potentially used for photonic applications for optical devices[17] and has been shown to exhibit shift currents in its ferroelectric phase.[18] The bulk Curie temperature for SbSI, however, is slightly below room temperature (~17–23°C), which renders it virtually unusable in applied technologies although it carries a sizable bulk spontaneous polarization of about 25 μC/cm^2 at 0°C.[19] Interestingly, due to recent strain-engineering efforts, it was found that strained SbSI microrods saw an increase of their Curie temperature by up to 70°C as evidenced by temperature-dependent photoluminescence spectroscopy.[9] This means that the promising optoelectronic properties of SbSI could be brought to industrial applications via such strain engineering. Because strain can also be used to drive phase transitions and tune bandgaps,[9,20] strain engineering the Curie temperature could have the added benefit of making SbSI an efficient water oxidation catalyst, where a bandgap of >2 eV is sought.[8]

Materials and methods

We performed in-house powder x-ray diffraction and transmission electron microscopy to structurally characterize our as-grown SbSI nanowires, confirming their phase purity and the general morphology of the system. More details of these measurements are given in our previous study.[9] This study reports transmission electron microscopy and Bragg coherent diffractive imaging (BCDI) reconstructions, as shown in **Figure 1**. In order to better guide strain-engineering efforts in the SbSI system, we performed strain mapping and crystalline quality assessment at the single nanowire level by employing BCDI. BCDI is a lensless imaging technique that employs coherent x-rays to collect three-dimensional (3D) Bragg diffraction patterns in the far field, which are then iteratively inverted to their (complex) real space equivalent.[21] The 3D Bragg peak collected for the wire reported here is displayed in Figure 1a, along with three of its projections. The solution resulting from the iterative phase retrieval bypasses the phase problem of x-ray crystallography, granting both scattering amplitudes and relative displacement of the scattering centers for a given Bragg plane. The (3D) reconstruction represents the crystal where the amplitude can be seen as the electronic population within the Bragg planes, and the phase is the atomic displacement field projected onto the reciprocal lattice vector.[21] The complex Bragg electronic density can be seen in Figure 1b, where the phase has been projected onto an isosurface of the amplitude, taken at 15% of the maximum amplitude. Spatial gradients of the projected displacement field yield some components of the strain tensor. Current state-of-the-art BCDI yields 3D spatial resolutions as high as ~4–9 nm and strain sensitivity of ~10^{-4}.[21,22] The BCDI technique is a promising tool to probe displacement and strain field in individual nanocrystalline materials. Previous studies have demonstrated the capability of BCDI in recovering the full strain tensor[23] by measuring 3D coherent diffraction patterns from multiple Bragg reflections (noncollinear Q-vectors). Having access to the full strain tensor leverages BCDI as an ideal technique to spatially resolve structure-property relationships. Other studies have outlined the applicability of BCDI in accessing strain in semiconductor nanowires[24] and unlocking associated effects such as elastic domains, spontaneous electric polarizations, and topological defects in complex nanocrystalline systems.[25–33]

We have successfully grown high-quality phase-pure SbSI nanowires via chemical vapor deposition (CVD). CVD of SbSI was performed in a tube furnace (Lindberg Blue M, Thermo Fisher Scientific, Inc.) using Sb_2S_3 (Sigma Aldrich) and SbI_3 (Sigma Aldrich) as precursors. Before the deposition, Sb_2S_3 powder was placed in a silica boat at the center of the heating zone, while SbI_3 powder was placed 10 cm away toward the upstream direction. Freshly cleaved mica (SPI) was used as the substrate. The growth temperature was 650 K. Prior to the heating up, the system was pumped down to ~0.5 Torr and a 30-sccm flow of Ar was used as carrier gas. During the deposition, the chamber pressure was maintained at ~100 Torr. The

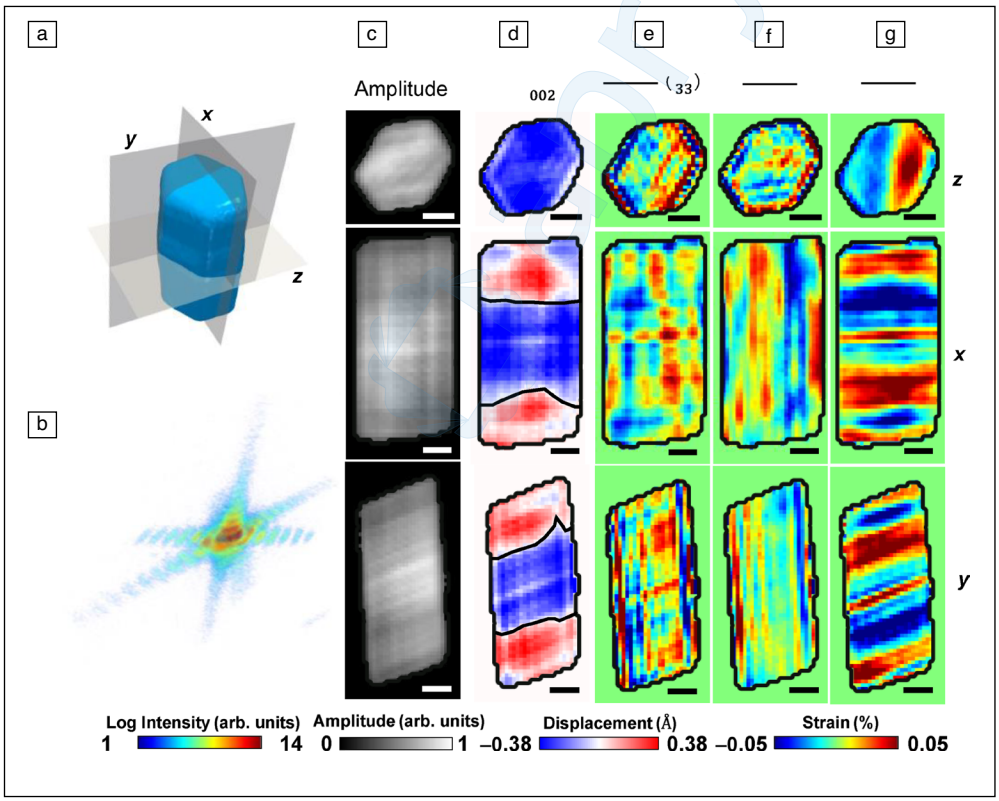

Figure 2. (a) Isosurface of the amplitude taken at 15% of the maximum with cut planes labeled for the images in (c–g). (b) Volumetric representation of the collected Bragg diffraction pattern, log scale (c–g) cut planes showing the quantities of (c) amplitude, (d) relative displacement of (002) planes, and (e–g) spatial gradients of the displacement (strain) for the *z*, *x*, and *y*-directions, respectively. Gradients are taken in the crystallographic directions ($\vec{a}$, $\vec{b}$, $\vec{c}$), which were identified based on the known [002] direction (wire axis) and previous studies illuminating the faceting in SbSI nanowire systems.[36] Scale bars = 100 nm.

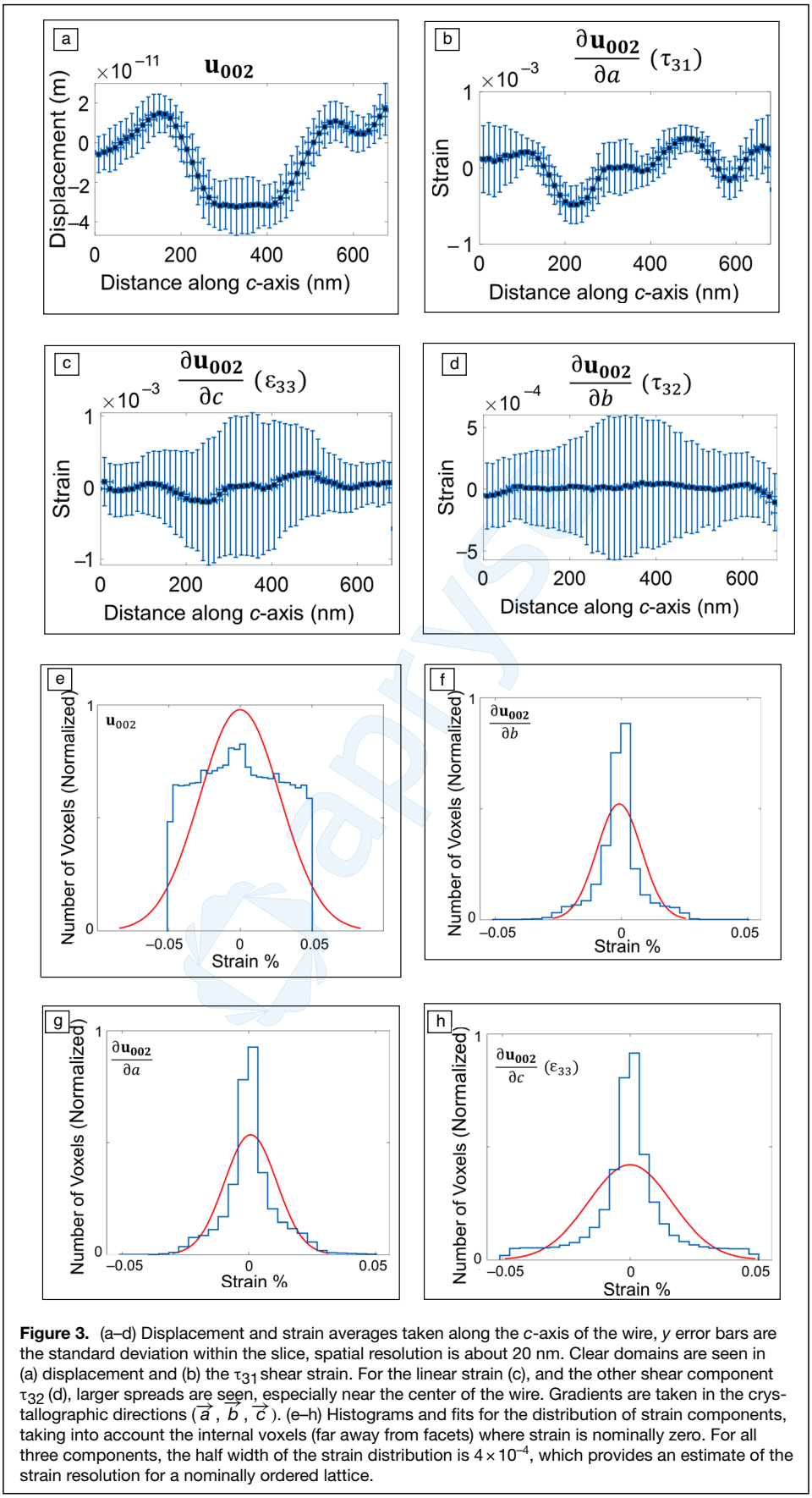

Figure 3. (a–d) Displacement and strain averages taken along the *c*-axis of the wire, *y* error bars are the standard deviation within the slice, spatial resolution is about 20 nm. Clear domains are seen in (a) displacement and (b) the τ_{31} shear strain. For the linear strain (c), and the other shear component τ_{32} (d), larger spreads are seen, especially near the center of the wire. Gradients are taken in the crystallographic directions ($\vec{a}$, $\vec{b}$, $\vec{c}$). (e–h) Histograms and fits for the distribution of strain components, taking into account the internal voxels (far away from facets) where strain is nominally zero. For all three components, the half width of the strain distribution is 4×10^{-4}, which provides an estimate of the strain resolution for a nominally ordered lattice.

deposition process lasted for ~40 min, and after cooling down, nanowires of SbSI were obtained on the mica substrates. After the growth, the synthesized SbSI nanowires should lie horizontally on the mica substrate. The SbSI nanowires were transferred to an SiO_2 template on Si for CDI measurement. Based on previous reports and our TEM results, the growth direction of nanowires should be along the *c*-axis/[001] of the SbSI unit cell. A 22° angle is seen in Figure 1b, as well as Figure 1c–d of the TEM images. From this we deduce the *c*-axis/[001] of the SbSI unit cell is tilted 22° with respect to the silicon substrate.

The wires are found to be in the paraelectric phase, with the *Pnam* space group, as reported previously (see Reference 9). Detailed descriptions of our synthesis and in-house characterizations were previously reported.[9] The sizes of the wires varied between roughly 50 nm to 10-μm wide and 300 nm to 100-μm long. We also observed from our previous studies using SEM that the cross sections of the nanowires are irregular. For the purpose of this study, we chose to image a nanowire that fit within the coherent volume of the x-ray beam (approximately 350 nm × 350 nm wide, and 700 nm long).

We collected a series of coherent Bragg diffraction patterns about the (002) reflection of an individual SbSI nanowire by rocking the crystal in 181 small angular increments (~0.005°) through the Bragg condition, effectively collecting the 3D Bragg diffraction pattern for the wire. The BCDI experiments were performed at room temperature. The experiments were performed at beamline 34-ID-C of the Advanced Photon Source using an x-ray energy of 9000 ± 1 eV, where the incident beam was focused using Kirkpatrick–Baez mirrors to a spot size of ~2 μm × 2 μm. Diffraction patterns were captured using a direct-detection charge-coupled device (CCD) (Roper/PI direct-detection CCD) with 20.5-μm square pixels located on the detector arm, 1.05 m away from the sample.

Reconstructions from the collected 3D Bragg diffraction patterns were performed using a combination of Fienup's Hybrid input–output (HIO) and error-reduction (ER) algorithms.[34] In-depth experimental details for similar BCDI experiments that we performed at 34-ID-C are given in References 27 and 35. The iterative reconstructions were performed with 30 iterations of ER, 300 iterations of HIO, and followed by 30 iterations of ER with a random amplitude and a flat phase for the initial starting guesses. The χ-square of the reconstructed data used here is ~0.02. To ensure and confirm the reproducibility and uniqueness of the reconstruction, we performed a series of iterative reconstruction procedures with different random starting guesses of the amplitude of the object.

Results and discussion

The 3D diffraction pattern shown in Figure 1a is highly symmetric with well-defined interference fringes, indicating a highly crystalline nanowire with low inhomogeneous strain and a hexagonal cross section. One obvious asymmetry presents itself in the lack of mirror symmetry in the interference fringes coming from the ends of the wire (or (011)-type facets) relative to the wire axis. In fact, there seems to be only one set of interference fringes coming from the ends of the wire, whereas an ideal SbSI nanowire should have six facets at its ends.[17] In the reconstruction, this manifests as single-faceted ends (the (011)-type) at an approximate 22° angle from the wire axis and a global tilt of the wire in the (100) direction. This agrees well with the known geometry of the SbSI unit cell. It is indicated already that the strain caused by enhanced surface energies in the nanowire could increase the Curie temperature. At the nanoscale, surfaces make up a significant portion of the volume of nanostructures and, therefore, contribute significantly to the total energy landscape. While this study was performed using a single Bragg reflection, BCDI allows one to measure the entire strain tensor for an individual nanostructure using at least three noncollinear Bragg reflections.[23] In future studies, we look to perform such a study in the SbSI system to better illuminate the role that strain from the surface facets affects the total energy landscape of the nanowires. In our recent studies on SbSl nanowires,[9] we observed (using Landau theory) an increase in the Curie temperature from ~300 K to ~360 K when the nanowire is subjected to mechanical stress. Also, due to the fact that multiple factors such as the crystalline strain, shape anisotropy, and facet energy all contribute to the potential energy landscape of our system, the observed change in Curie temperature depends ultimately on a delicate balance between these parameters. We expect that experiments in which (hydrostatic) strain is applied can potentially alter functional properties such as shifting of the energy levels relative to the unstrained conduction and valence bands. Also the presence of uniaxial and biaxial strain can lift the band degeneracy in such low bandgap materials. Our future experiments will, thus, require (1) SbSI nanowires with a variety of shapes, (2) accessing multiple reflections from each individual nanowire, (3) performing BCDI on SbSI nanowires under external perturbations such as temperature and mechanical load, and (4) developing a Landau model to interpret our BCDI experimental observation.[9]

In earlier studies,[17] six facets were observed in SbSI. Here, using low-magnification transmission electron micrographs in Figure 1c–d where 3D information is muddled, such facet selectivity could not be gleaned from the data. Figure 1e shows selected-area electron diffraction from an individual wire. In Figure 1c–d, we index the observed diffractions and our results align with its expected unit cell.[36]

A summary of the reconstructed structure and morphology of the SbSI nanowire is displayed in **Figure 2**. Figure 2a shows an isosurface of the amplitude taken at 15% of the maximum, with slice planes labeled for the images in Figure 2c–g. A volume representation of the coherent Bragg diffraction pattern (log scale) is shown in Figure 2b. The reconstructed nanowire is found to have well-defined facets, with near homogeneous electronic population of the Bragg planes with some striped variation occurring along the *c*-axis, where regions of high electronic density are found to slightly

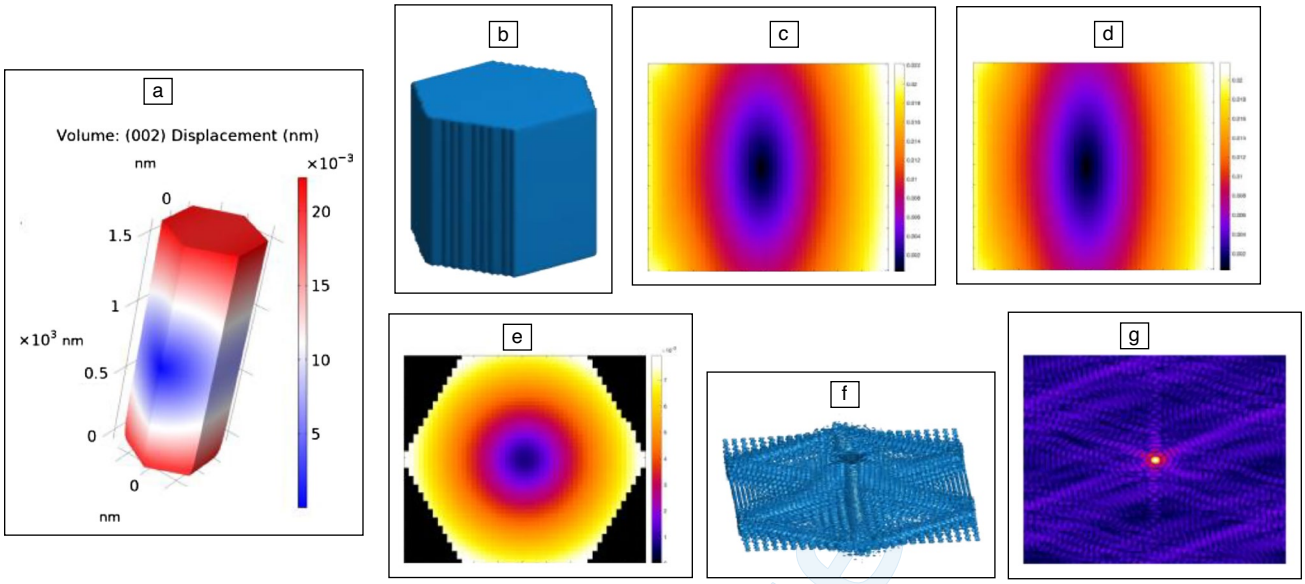

Figure 4. COMSOL multiphysics finite element analysis (FEA) simulation of ferroelastic domains under influence of surface strains. (a) (002) displacement (nm) of the nanowire as a result of application of an equal pressure on each face of 2 MPa. (b) Three-dimensional (3D) amplitude of the nanowire for the FEA simulation. (c–e) (002) displacement in nm of the central slice of the nanowire in the two lateral and the *c*-axis directions, respectively. (f) Simulated 3D diffraction intensity of the nanowire in (a). (g) Central slice of the simulated diffraction intensity in (a).

bulge at the center of the nanowire. This bulged center of the nanowire has a negative displacement relative to either end of the nanowire, with the nanowire split into three domains. Our beam focal size is around ~2 μm × 2 μm; therefore, the size of our nanowire is only a fraction of the beam spot, and we expect the beam profile variation in the illumination area of the nanowire to be relatively flat. We hypothesize these displacement domains are signs of polarization domains, suggesting that the crystal is in the ferroelectric phase at room temperature. The entire displacement has relatively smooth variation inside each of the three strain domains, indicating the absence of substantial line or plane defects,[37] apart from the domain walls, which separate regions with about 0.5 Å relative displacement difference between them. We observe in Figure 2d that, there is a maximum displacement of about 0.76 Å within the nanowire. Along the length of the wire (Figure 2d), we identify three distinct elastic domain regions with averagely uniform displacements.

The reconstruction also indicates a global tilt of the nanowire as the two parallel ends of the nanowire are not vertically aligned. The nanowire is found to grow about 22° off vertical (out-of-plane of the substrate), consistent with (011)-type facets in the SbSI crystal structure. The tilt in the nanowire likely results in a large number of dangling bonds on the surface of the wire, which in turn, could influence the strain state of the wire, creating an opportunity for strain engineering. The shear strain component displayed in Figure 2g indicates shear domains, where the domain boundaries appear parallel to the (011)-type facets. The ferroelectric polarization in SbSI typically appears along the *c*-axis, whereas this shear component is insensitive to linear strain along the *c*-axis. Therefore, these domains should be completely independent of the ferroelectric polarization, and we conclude that these are likely elastic domains that form to minimize the strain energy coming from the surface strains in the wire. Line plots of the quantities shown in Figure 2d–g are plotted in **Figure 3**a–d. The data points in these line plots are found by slicing along the *z*-axis shown in Figure 2a (the *c*-axis), and averaging the voxels contained within the support of the reconstruction. Vertical error bars are assigned as the standard deviation of these voxels, and the horizontal error bars are set as the lateral resolution, ~20 nm. Domains are apparent in Figure 3a atomic displacement and (b) shear strain component τ_{31}. The presence of displacement domains in the absence of long-range tensile/compressive strain field is easily explained via the structural distortion accompanying ferroelectric domains. The asymmetry between the τ_{31} and τ_{32} shear components is evidence of another influence on the strain state of the system, consistent with the proposed surface strain effects. While the ideal SbSI nanowires are expected to have hexagonal-shaped facets at the tips, the asymmetry of the coherent fringes observed in the diffraction pattern is mostly due to the strain within in the nanowire. This strain will potentially alter the nature of the ferroelectric and elastic domains. The observed domains are predominantly ferroelastic in nature (as opposed to twin domains) due to the absence of twinned diffraction.

We analyzed and added the histograms with fittings as a function of strain (Figure 3e–h) for Figure 2d, relative displacement of (002) planes, and Figure 2e–g spatial gradients of the displacement (strain) for the *x*, *y*, and *z*-directions, respectively. The domains are predominantly ferroelastic as we did

not observe any charcteristic twin diffraction from the BCDI measurements. These are ferroelastic domains that we believe are indicative of ferroelectric domains. This is similar to previous work on ferroelectric systems (see Reference 27). Regarding twins specifically, coherent diffraction peaks from twinned crystals have distinct reciprocal space features, including split peaks that were not present in this sample. More information on twins in coherent diffraction can be found in Reference 38.

We have performed finite element analysis (FEA) simulation studies using COMSOL multiphysics.

To demonstrate how surface strain can result in elastic domains, such as those presented here, we performed a FEA of a model system using COMSOL multiphysics. A single SbSI wire was modeled as an isotropic solid with a surface strain created by an equal pressure on each face of 2 MPa. The results of this analysis are summarized in **Figure 4**. This model is limited due to both the assumption that the material behaves isotropically and that each surface experiences equal strain. However, the model shows good agreement with our experimental results, suggesting that these assumptions when taken together do not invalidate the use of this model to demonstrate how surface strain leads to elastic domains such as those imaged here.

In T-phase ferroelectrics (e.g., T-phase BTO), ferroelastic domain walls can mediate a 90° rotation of the ferroelectric polarization. However, to conclude on the FE domain, it is necessary to cycle the sample under an external electric field.[27] Furthermore, to conclude in the ferroelastic domain, it is required to cycle the system under applied stress.[35] For more information, please refer to the detailed studies, relating to polarization, in our previous publication.[35]

Summary

With a strain resolution of ~10^{-4}, we found that the tensile/compressive strain along the *c*-axis in our measured SbSI nanowire is relatively low compared to the shear strain. A global tilt present in the nanowire likely opens dangling bonds on the lateral facets, granting greater bonding opportunity for strain-engineering shells, which can bring the Curie temperature for SbSI above room temperature. Indeed, the wire seems bulged near the center as evidenced by the Bragg electronic density, indicating excess SbSI growth there and possibly explaining more complex morphologies observed in SbSI growth such as urchins.[17] Atomic displacement along the [001] direction hints that ferroelectric domains could be present in the wire already above room temperature, which could be stabilized due to the excess strain energy coming from the high surface/volume ratio in the nanoscale wire. We have also identified elastic shear domains present in the τ_{31} shear strain component for the nanowire, which we attribute to minimizing strain energy coming from the facets of the wire. We hope that our strain mapping efforts help guide future strain-engineering attempts on SbSI to utilize its favorable optical properties in above room-temperature optoelectronic devices.

Acknowledgments

E.F. and J.S. acknowledge support from the US Department of Energy, Award No. DE-SC0023148, and from the National Science Foundation under Award No. 2024972. E.F. also acknowledges funds from Rensselaer Polytechnic Institute. This research used resources of the Advanced Photon Source (APS), a US Department of Energy (DOE) Office of Science User Facility operated for the DOE Office of Science by Argonne National Laboratory (ANL) under Contract No. DE-AC02-06CH11357. We thank the staff at ANL and the APS for their support.

Data availability

The data are available both at the Advanced Photon Source and upon request from the corresponding author.

Competing interests

The authors declare no competing financial interests.

References

1. L. Lv, F. Zhuge, F. Xie, X. Xiong, Q. Zhang, N. Zhang, Y. Huang, T. Zhai, *Nat. Commun.* **10**, 3331 (2019)
2. Z.-D. Luo, X. Xia, M.-M. Yang, N.R. Wilson, A. Gruverman, M. Alexe, *ACS Nano* **14**, 746 (2020)
3. S. Rühle, *Sol. Energy* **130**, 139 (2016)
4. L.Z. Tan, F. Zheng, S.M. Young, F. Wang, S. Liu, A.M. Rappe, *NPJ Comput. Mater.* **2**(1), 16026 (2016)
5. S.Y. Yang, J. Seidel, S.J. Byrnes, P. Shafer, C.-H. Yang, M.D. Rossell, P. Yu, Y.-H. Chu, J.F. Scott, J.W. Ager III, L.W. Martin, R. Ramesh, *Nat. Nanotechnol.* **5**, 143 (2010)
6. R. Nechache, C. Harnagea, S. Li, L. Cardenas, W. Huang, J. Chakrabartty, F. Rosei, *Nat. Photonics* **9**, 61 (2015)
7. R. Guo, L. You, Y. Zhou, Z. Shiuh Lim, X. Zou, L. Chen, R. Ramesh, J. Wang, *Nat. Commun.* **4**, 1990 (2013)
8. N. Vonrüti, U. Aschauer, *J. Mater. Chem. A* **7**, 15741 (2019)
9. Y. Wang, Y. Hu, Z. Chen, Y. Guo, D. Wang, E.A. Wertz, J. Shi, *Appl. Phys. Lett.* **112**, 183104 (2018)
10. A.S. Bhalla, R.E. Newnham, L.E. Cross, J.P. Dougherty, W.A. Smith, *Ferroelectrics* **33**, 3 (1981)
11. M. Nowak, P. Szperlich, *Opt. Mater.* (Amst) **35**(6), 1200 (2013)
12. K. Mistewicz, M. Nowak, D. Stróż, *Nanomaterials* **9**, 13 (2019)
13. B. Garbarz-Glos, J. Grigas, *Ferroelectrics* **393**, 38 (2009)
14. R. Nie, H. Yun, M.-J. Paik, A. Mehta, B. Park, Y.C. Choi, S. Il Seok, *Adv. Energy Mater.* **8**, 1701901 (2018)
15. K. Mistewicz, M. Nowak, D. Stróż, A. Guiseppi-Elie, *Talanta* **189**, 225 (2018)
16. J. Shen, X. Liu, C. Wang, J. Wang, B. Wu, X. Chen, G. Yi, *J. Phys. D* **53**, 345106 (2020)
17. M. Tamilselvan, A.J. Bhattacharyya, *RSC Adv.* **6**, 105980 (2016)
18. N. Ogawa, M. Sotome, Y. Kaneko, M. Ogino, Y. Tokura, *Phys. Rev. B* **96**, 241203 (2017)
19. E. Fatuzzo, G. Harbeke, W.J. Merz, R. Nitsche, H. Roetschi, W. Ruppel, *Phys. Rev.* **127**, 2036 (1962)
20. Y. Wang, X. Sun, Z. Chen, Z. Cai, H. Zhou, T.-M. Lu, J. Shi, *Sci. Adv.* **4**, eaar3679 (2018)
21. D. Karpov, E. Fohtung, *J. Appl. Phys.* **125**, 121101 (2019)
22. M.J. Cherukara, W. Cha, R.J. Harder, *Appl. Phys. Lett.* **113**, 203101 (2018)
23. M.C. Newton, S.J. Leake, R. Harder, I.K. Robinson, *Nat. Mater.* **9**, 120 (2010)
24. D. Dzhigaev, A. Shabalin, T. Stankevič, U. Lorenz, R.P. Kurta, F. Seiboth, J. Wallentin, A. Singer, S. Lazarev, O.M. Yefanov, M. Borgström, M.N. Strikhanov, L. Samuelson, G. Falkenberg, C.G. Schroer, A. Mikkelsen, R. Feidenhans'l, I.A. Vartanyants, *J. Opt.* **18**(6), 064007 (2016)
25. J. Diao, X. Shi, T.A. Assefa, L. Wu, A.F. Suzana, D.S. Nunes, D. Batey, S. Cipiccia, C. Rau, R.J. Harder, W. Cha, I.K. Robinson, *Phys. Rev. Mater.* **4**(10), 106001 (2020)
26. N. Laanait, W. Saenrang, H. Zhou, C.-B. Eom, Z. Zhang, *Adv. Struct. Chem. Imaging* **3**, 11 (2017)
27. D. Karpov, Z. Liu, T.S. dos Rolo, R. Harder, P.V. Balachandran, D. Xue, T. Lookman, E. Fohtung, *Nat. Commun.* **8**, 280 (2017)
28. D. Karpov, Z. Liu, A. Kumar, B. Kiefer, R. Harder, T. Lookman, E. Fohtung, *Phys. Rev. B* **100**, 54432 (2019)
29. J.W. Kim, S. Manna, R. Harder, J. Wingert, E.E. Fullerton, O.G. Shpyrko, *J. Appl. Phys.* **123**, 204302 (2018)

30. J. Logan, R. Harder, L. Li, D. Haskel, P. Chen, R. Winarski, P. Fuesz, D. Schlagel, D. Vine, C. Benson, I. McNulty, *J. Synchrotron Radiat.* **23**, 1210 (2016)
31. S. Manna, J.W. Kim, M.V. Lubarda, J. Wingert, R. Harder, F. Spada, V. Lomakin, O. Shpyrko, E.E. Fullerton, *AIP Adv.* **7**, 125025 (2017)
32. E. Fohtung, "Magnetostriction Fundamentals," in *Encyclopedia of Smart Materials,* ed. by A.-G. Olabi (Elsevier, Oxford, 2022), pp.130–133
33. A. Pateras, R. Harder, S. Manna, B. Kiefer, R.L. Sandberg, S. Trugman, J.W. Kim, J. de la Venta, E.E. Fullerton, O.G. Shpyrko, E. Fohtung, *NPG Asia Mater.* **11**, 59 (2019)
34. J.R. Fienup, *Appl. Opt.* **21**, 2758 (1982)
35. Z. Liu, E. Schold, D. Karpov, R. Harder, T. Lookman, E. Fohtung, *Adv. Electron. Mater.* **6**, 1901300 (2020)
36. A. Kikuchi, Y. Oka, E. Sawaguchi, *J. Phys. Soc. Jpn.* **23**, 337 (1967)
37. Z. Barringer, J. Jiang, X. Shi, E. Schold, A. Pateras, S. Cipiccia, C. Rau, J. Shi, E. Fohtung, *CrystEngComm* **23**(36), 6239 (2021)
38. M.A.G. Aranda, F. Berenguer, R.J. Bean, X. Shi, G. Xiong, S.P. Collins, C. Nave, I.K. Robinson, *J. Synchrotron Radiat.* **17**, 751 (2010) □